Materials Advances

ROYAL SOCIETY OF CHEMISTRY

PAPER

View Article Online
View Journal

Cite this: DOI: 10.1039/d6ma00229c

Bridging energy conversion and storage: precursor-engineered Co@CoO–Y_2O_3 heterostructures for oxygen reduction reaction and battery-type supercapacitor applications

Sukhendu Bikash Samanta,†[a] Soumalya Roy,†[b] Sudipta Palit,[a] Joshi Ankitkumar Bharatbhai,[a] Nishipadma Barik,[c] Himchan Mo,[b] Junseong Lee,*[b] Soumen Giri *[cde] and Sourav Das*[a]

The escalating consumption of fossil fuels and the intermittency of renewable power have intensified the need for multifunctional electrochemical materials that can couple efficient energy conversion and durable energy storage while avoiding device-level complexity and reliance on Pt. Herein, we report a non-noble metal-based Co@CoO–Y_2O_3 (CCY) heterostructured composite synthesized *via* the pyrolysis of a well-defined cobalt–yttrium single-crystal precursor complex. Structural and spectroscopic analyses confirm the coexistence of metallic Co, CoO, and Y_2O_3 phases, with strong Co–O–Y interfacial coupling and oxygen-vacancy-rich heterointerfaces arising from rare-earth oxide incorporation. The CCY composite exhibited hierarchical mesoporosity, facilitating mass transport and active site accessibility. In alkaline media (1 M KOH), CCY demonstrates competitive oxygen reduction reaction (ORR) activity, delivering a half-wave potential of 0.603 V (*vs.* RHE), an onset potential of 0.79 V, and stable operation for over 24 h. Koutecky–Levich analysis indicates a predominantly two-electron ORR pathway with high peroxide selectivity, highlighting its suitability for non-Pt catalytic systems. Simultaneously, when employed as a battery-type supercapacitor electrode, CCY exhibited electrolyte-dependent faradaic charge storage, achieving specific capacitances of 22, 18.74, and 10.12 F g^{-1} at 0.1 A g^{-1} in KOH, NaOH, and LiOH electrolytes, respectively, along with a low charge-transfer resistance and ~64.14% capacitance retention over 10 000 cycles. The incorporation of Y_2O_3 stabilizes the Co@CoO framework by suppressing cobalt dissolution and inducing interfacial electronic modulation and oxygen vacancy formation. This study establishes a scalable, precursor-driven strategy for designing rare-earth-modified bifunctional materials for integrated energy conversion and storage applications.

Received 17th February 2026,
Accepted 30th April 2026

DOI: 10.1039/d6ma00229c

rsc.li/materials-advances

1. Introduction

The global transition toward renewable energy systems has intensified the demand for advanced materials capable of mitigating power intermittency while enabling efficient energy conversion and storage.[1,2] In this context, multifunctional electrochemical materials with combined catalytic performance and rapid charge–discharge properties have been recently proposed as they are believed to be more efficient in terms of overall system-level performance by avoiding device complexity.[3,4] Among various technologies, metal–air batteries, proton exchange membrane fuel cells (PEMFCs), and battery-type supercapacitors have drawn special attention because of their high power density, environmental benignancy, and theoretical energy densities, which significantly surpass those of conventional lithium-ion batteries.[5]

The oxygen reduction reaction (ORR), which occurs at the cathode of fuel cells and metal–air batteries (Li, Na, K, Zn, Mg, and Al–air systems), is a key rate-limiting step that governs the overall device efficiency.[6] The ORR can proceed *via* two distinct pathways: a direct four-electron pathway ($O_2 + 2H_2O + 4e^- \rightarrow 4OH^-$)

[a] Department of Basic Sciences, Chemistry Discipline, Institute of Infrastructure Technology, Research and Management (IITRAM), Ahmedabad, Gujarat, India. E-mail: souravdas@iitram.ac.in
[b] Department of Chemistry, Chonnam National University, 77 Yongbong-ro, Buk-gu, Gwangju 61186, Korea. E-mail: leespy@chonnam.ac.kr
[c] School of Applied Sciences, Kalinga Institute of Industrial Technology (KIIT) Deemed to be University, Bhubaneswar-751024, Odisha, India. E-mail: soumen.girifch@kiit.ac.in
[d] Centre of Innovation and Research-Electrical Vehicle (COIR-EV), KIIT Deemed to be University, Bhubaneswar 751024, Odisha, India
[e] Centre of Innovation and Research-Next-Generation Materials and Technology (COIR-CNGMT), KIIT Deemed to be University, Bhubaneswar 751024, Odisha, India
† These authors contributed equally to this work.

that is thermodynamically and kinetically favorable, or a less efficient two-electron pathway ($O_2 + H_2O + 2e^- \rightarrow HO_2^- + OH^-$; $HO_2^- + H_2O + 2e^- \rightarrow 3OH^-$) involving the formation of peroxide intermediates. The sluggish kinetics of the ORR significantly limit the efficiency of PEMFCs and metal–air batteries, necessitating the development of highly active electrocatalysts.[7] Although Pt-based catalysts are also standards for ORR activity, their high cost and limited availability, accounting for ~20% of the PEMFC system costs, have greatly hindered their broad industrialization.[8] This has driven much research in the area of earth-abundant, non-noble metal alternatives.

Recent advances have demonstrated that rare-earth (RE) oxide-modified transition metal oxides (TMOs) can rival or even surpass Pt/C in alkaline media. From 2023 to 2025, several significant systems have been identified, such as CeO_2/Fe_3C@N-C heterostructures, Y_2O_3-decorated Fe–N_4/Fe_4N nanoclusters, and Er_2O_3–Co composites exhibiting spin-selective coupling. These systems have achieved half-wave potentials approaching or exceeding those of Pt/C, with excellent durability.[9–11] These results highlight the specialized role of RE elements, which possess partially filled 4f orbitals, exhibit low electron affinity, and have multiple degenerate states that facilitate interfacial charge redistribution and optimized adsorption energetics.[12,13] The incorporation of RE oxides (*e.g.*, Y_2O_3, La_2O_3, CeO_2, Er_2O_3, and Dy_2O_3) into TMO matrices leads to synergistic effects, including (i) electronic modulation facilitated by the interfacial coupling between RE and O-TM, (ii) the creation of oxygen vacancies that boost ORR kinetics, (iii) the inhibition of nanoparticle agglomeration, and (iv) spin/orbital interactions that decrease reaction energy barriers.[9,14,15] In particular, Y_2O_3 effectively tunes the Co d-band centers owing to its Lewis acidity and high oxygen vacancy formation energy, while La_2O_3 enhances the interfacial electron density through TM–O–RE catalytic motifs, collectively improving the activity and durability.[10,16,17]

In addition to catalytic energy conversion, battery-type supercapacitors have gained increasing attention as intermediate energy storage systems that bridge the gap between batteries and conventional capacitors.[18] Unlike traditional electrostatic double-layer capacitors, battery-type electrodes store energy *via* fast surface or near-surface faradaic reactions, thereby providing higher density without losing power capability. TMOs, including Co, V, and Ti, have demonstrated great potential, with their performance depending closely on morphology variation and heterointerface engineering, as well as electronic modulation.[19–21] Notably, several materials have been engineered to deliver dual functionality, serving as efficient electrocatalysts for the ORR/OER and as high-performance pseudocapacitive or battery-type storage electrodes. Representative examples include $Co_3V_2O_8$ microstructures (areal capacitance of 3.76 F cm^{-2} at 1 mA cm^{-2}) with bifunctional water-splitting activity and CuCo-LDH@Ni heterostructures exhibiting ultrahigh capacitance (15.43 F cm^{-2} at 5 mA cm^{-2}) alongside strong HER/OER performance, paving the way for the development of integrated self-powered systems.[2,4]

The synthesis of multifunctional materials using precisely characterized precursor complexes has emerged as an appealing strategy for the controlled preparation of morphologies, compositions, and surface areas that are often superior to those of bulk analogues.[22] In this context, coordination-complex-derived bimetallic systems have demonstrated significant promise. For instance, Cu–Co sulfides synthesized *via* a well-defined precursor route exploit synergistic dual-metal-ion effects to deliver enhanced battery-type supercapacitor performance.[23] Similarly, anion exchange in CuCo-carbonate double hydroxides has been shown to effectively tune faradaic charge storage behavior in hybrid supercapacitors.[24] More recently, nanostructured Cu_3P–CoP cathodes with a 3D urchin-like morphology, fabricated through a coordinated precursor strategy, have achieved high energy and power densities in hybrid devices.[25] These studies collectively highlight the critical role of precursor engineering, morphology control, and heterointerface design in advancing next-generation electrode materials. MOF-derived and complex-derived pyrolysis methods can be employed to customize the interface architecture, oxygen vacancy concentration, and hierarchical pore structure with high-density active sites to achieve excellent electrocatalytic performance.[26,27] For instance, MOF-derived Co/CoO@NC-CNT hybrids with well-controlled oxygen vacancy content and interconnected carbon nanotube networks have been found to exhibit ORR half-wave potentials of 0.88 V (*vs.* RHE) and an onset potential of 0.96 V, even outperforming 20 wt% Pt/C in some studies.[28] Similarly, dopant-assisted nanocluster-making methods, such as the addition of Y_2O_3 containing Fe–N_x sites, lead to two active-site architectures by combining single atoms and nanoclusters, which can maximize the intrinsic activity and mass transport.[11] These synthesis strategies highlight the significance of interface-induced activity, defect engineering, and multiphase architectures in the development of next-generation electrocatalysts and energy storage materials. However, it remains challenging to scale up the synthesis from bulk materials to achieve uniform dispersion of RE nanoclusters or atomic sites, stability against alkaline environments beyond long term, and translation of this concept to practical electrodes with realistic mass loadings.[11,29]

Inspired by recent advances in rare-earth-modified transition metal oxides and the advantages of precursor-engineered synthesis, we report a dual-functional Co@CoO–Y_2O_3 (CCY) composite derived from a well-defined cobalt-yttrium precursor complex for simultaneous oxygen reduction and battery-type energy storage applications. According to the fundamental definition of capacitance,[30] pseudocapacitance represents a charge storage mechanism involving fast and reversible faradaic redox reactions occurring at the surface or near-surface of the electrode materials.[31] In true pseudocapacitive systems, the faradaic reactions proceed with very fast kinetics and without significant phase transformation, resulting in an electrochemical response similar to that of capacitors. Consequently, pseudocapacitive electrodes typically exhibit a quasi-rectangular cyclic voltammetry (CV) profile, a linear relationship between stored charge and applied potentials, and nearly linear galvanostatic charge–discharge (GCD) curves, analogous to electric double-layer capacitors (EDLCs). In contrast, when pronounced redox peaks appear in the CV curves and the GCD curves exhibit clear

voltage plateaus, the charge storage process is dominated by battery-type faradaic reactions rather than true pseudocapacitive behavior. Such electrochemical signatures indicate diffusion-controlled redox processes and phase transformations that are characteristic of battery-type electrodes. Therefore, materials showing distinct redox peaks and non-linear discharge profiles cannot be strictly classified as pseudocapacitive materials but instead behave as battery-type supercapacitor electrodes. Based on these electrochemical characteristics, it is more appropriate to express the electrochemical performance of such materials in terms of specific capacity (C g^{-1} or mAh g^{-1}) rather than specific capacitance (F g^{-1}), since the charge storage mechanism is governed by battery-type faradaic reactions instead of ideal capacitive behavior.[32] Now, in the present work, the system consisting of a cobalt metal core with a CoO surface and a heterointerface with Y_2O_3 also exhibits a similar kind of behavior to be called a battery-type supercapacitor electrode. The employment of a structurally defined precursor endows the system with high reproducibility and enables the controllable *in situ* formation of Co@CoO–Y_2O_3 heterointerfaces with desired electronic coupling and defects. As a result, the CCY hybrid presents effective ORR activity under alkaline conditions, which is characterized by the performance with a half-wave potential of ~0.603 V (*versus* RHE), onset potential at 0.79 V and durability for over 24 h without apparent current decay. In parallel, CCY functions as a battery-type supercapacitor electrode, achieving specific capacitances of 22, 18.74, and 10.12 F g^{-1} at 0.1 A g^{-1} in KOH, NaOH, and LiOH electrolytes, respectively, with ~64.14% capacitance retention after 10 000 cycles (KOH@1 Ag^{-1}). The incorporation of Y_2O_3 plays a critical role in stabilizing the Co@CoO framework by inducing synergistic electronic modulation and oxygen vacancy formation, thereby enhancing both the catalytic activity and long-term electrochemical durability. This study demonstrates a scalable precursor-driven strategy for designing multifunctional rare-earth-modified composites capable of addressing the coupled demands of energy conversion and storage in sustainable energy systems.

2. Experimental section

2.1. Chemicals and materials

In this work, the required chemicals were used as received, of analytical grade; no further purification was carried out. Pyridine-2,6-diyldimethanol (98%, 1195-59-1), 2-amino phenol (99%, 95-55-6), $CoCl_2{\cdot}6H_2O$ (99.9%, 7791-13-1), $Co(NO_3)_2{\cdot}6H_2O$ (99.9%, 10026-22-9), $YCl_3{\cdot}6H_2O$ (99.9%, 10025-94-2), $Y(NO_3)_3{\cdot}6H_2O$ (99.8%, 13494-98-9) and triethyl amine were purchased from Merck, India. Reagent-grade solvents were distilled under a nitrogen atmosphere before use.

2.2. Material preparation

2.1.1. Preparation of LH_2 [2,2′-{(1*E*,1′*E*)-pyridine2,6-diyl-bis(methaneylylidine)}-bis(azaneylylidine)diphenol]. A revised version of a previously documented method was employed to synthesize the highly pure yellow ligand, H_2L.[33,34]

2.1.2. Synthesis of the complex ($[Y(L)_2(Co)_2(Cl)_2(CH_3OH)_4]{\cdot}Cl{\cdot}3CH_3OH{\cdot}CHCl_3$). Red block-shaped crystals were synthesized by applying a previously established method that involved the use of the ligand H_2L.[35]

2.1.3. Preparation of the Co@CoO–Y_2O_3 (CCY) composite. Approximately 600 mg of the synthesized precursor complex was placed in an alumina boat and annealed in a tubular furnace under a 95% argon atmosphere at 800 °C for 8 h, using a heating rate of 3 °C min^{-1}. After completion of the thermal treatment, the furnace was allowed to cool naturally to room temperature, yielding a black-colored CCY composite powder. The final mass of the obtained product was ~120 mg. The overall synthesis procedure is schematically illustrated in Fig. 1.

2.1.4. Preparation of Y_2O_3. About 400 mg of yttrium(III) nitrate hexahydrate was placed in an alumina boat and annealed in the tubular furnace under air at 800 °C for 8 h, with a heating rate of 3 °C min^{-1}. After thermal treatment, the furnace cooled naturally to room temperature, yielding black-colored Y_2O_3 powder. The final mass of the product was ~150 mg.

2.1.5. Preparation of Co_3O_4. Approximately 400 mg of cobalt(II) nitrate hexahydrate was placed in an alumina boat and subjected to annealing in the tubular furnace under air at 800 °C for 8 h, with a heating rate of 3 °C min^{-1}. After thermal treatment, the furnace was allowed to cool naturally to room temperature, resulting in black-colored Co_3O_4 powder. The mass of the product was ~140 mg.

2.1.6. Preparation of physical mixing of Co_3O_4 + Y_2O_3. The Y_2O_3 powder and Co_3O_4 powder were mixed in a 1 : 1 ratio (wt/wt) homogeneously in a mortar and the prepared mixture was designated as Co_3O_4 + Y_2O_3 PM.

2.3. Characterization and instruments

The phase composition and crystal structure of the as-prepared CCY composites were analysed using a Malvern Panalytical Empyrean powder X-ray diffraction (XRD) instrument. X-ray photoelectron spectroscopy (XPS) was performed to elucidate the surface chemical states and elemental composition of the CCY composite material by using a Kratos Axis Ultra DLD spectrometer. The morphology and surface properties of the CCY composite were further studied using SEM (TESCAN Vega3 Model, 25.0 kV) and TEM (Philips EM208S Model). For BET analysis, the CCY composite was pretreated at 120 °C for 2 h. The Belsorp mini (JAPAN) and Finetec devices were employed at 77 K for analysing the adsorption–desorption isotherm of the synthesized composite. Raman spectroscopy was also performed for investigating lattice vibrational features and local structural disorders in the CCY composite using Bruker Raman spectrometers.

2.4. Electrochemical measurement

2.4.1. Electrode preparation

2.4.1.1. Preparation of the ink for the ORR. The catalyst ink for coating a glassy carbon (GC) disk electrode was prepared by using 2 mg of the catalyst, which was diluted in 500 μL solution

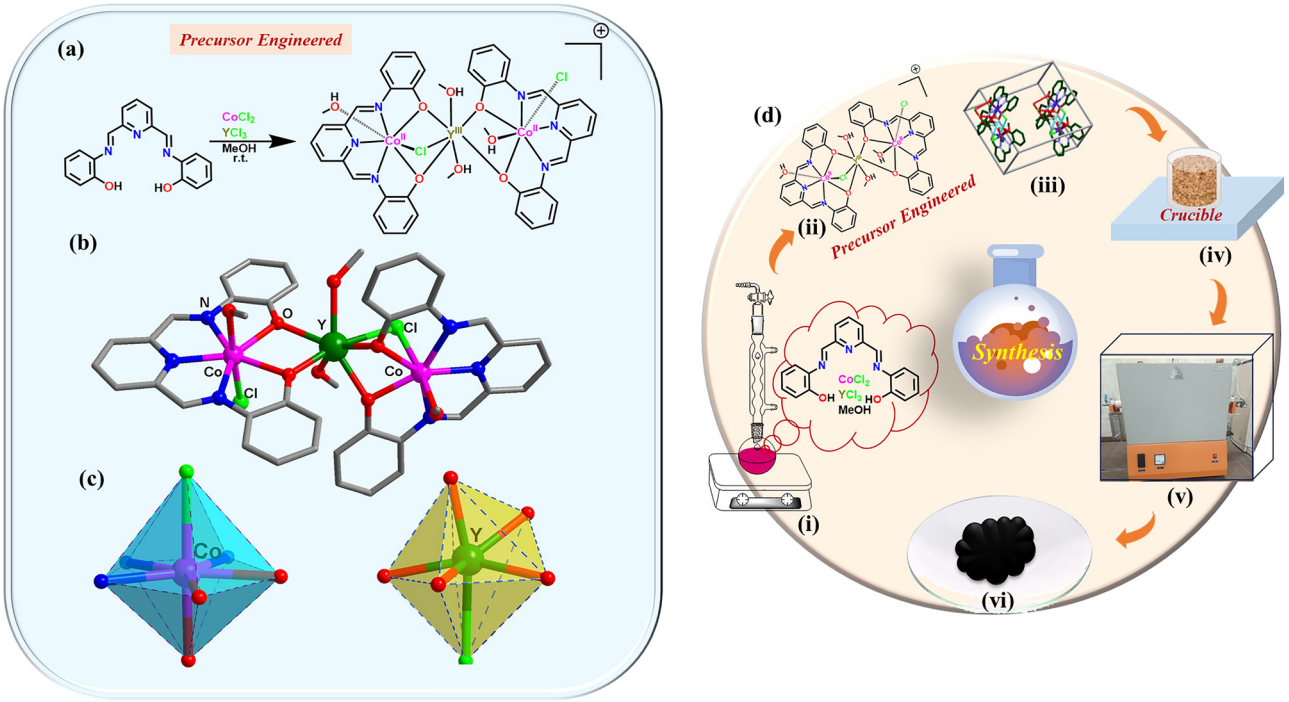

Fig. 1 (a) Synthetic diagram of precursor preparation,[28] (b) ball stick model of precursor (all noncoordinating H atoms is not considered), (c) Co and Y coordinated with the geometry of distorted pentagonal bi-pyramidal, and (d) schematic diagram of the synthesis of Co@CoO–Y_2O_3 from the precursor [stepwise (i) precursor preparation, (ii) precursor molecular structure, (iii) asymmetric unit of the complex, (iv) load into a crucible, (v) tubular furnace, and (vi) product after pyrolysis].

that was prepared using water, NMP, and Nafion (7.5 : 2 : 0.5 ratio). Nafion was used as the binder. The ink was sonicated well to prepare a homogeneous mixture, and 7.5 μL was drop-cast over the electrode and dried at room temperature for 8 h. The loading of the catalyst on the GC electrode surface was 0.25 mg cm^{-2} (0.03 mg coated on 0.125 cm^2).

All electrochemical experiments were performed using a CorrTest Potentiostat (Model Number: CS2350). For ORR measurements, a potentiostat was coupled to a rotating ring disk electrode (RRDE) [ALS, Japan]. A glassy carbon (GC) disk electrode (0.125 cm^2 surface area) was used as the working electrode, Hg/HgO [saturated in 1(M) KOH] was used as a reference electrode, and a graphite rod was used as a counter electrode, which was purchased from CorrTest India. Before any measurement, the GC electrode surface was polished with Al_2O_3 suspension and washed several times with Millipore water. All electrochemical experiments were performed in 1 (M) KOH solution. All the LSV curves were obtained at a scan rate of 5 mV s^{-1}. The same scan rate was also applied to obtain the different rotation rates (100–2500 rpm).

2.4.1.2. Preparation of the ink for supercapacitor experiments. A standard coating technique was employed to apply the catalyst onto Ni-foam, which served as the working electrode for the supercapacitor experiment. First, a (1 cm × 1 cm) Ni-foam was cleaned and activated. These involved the following steps-

(i) Ni-foam was sonicated with 4(M) HCl for 15 min and washed with Millipore water.

(ii) The mixture was sonicated with acetone for 10 min and washed with Millipore water.

(iii) Next, the samples were sonicated in ethanol for 10 min and washed with Millipore water.

(iv) Finally, the mixture was sonicated with Millipore water for 10 min.

The Ni foam was then dried in a hot oven at 75 °C for 30 min. Next, the catalyst was mixed with Super-P and PVDF (7 : 2 : 1 ratio) and a paste was prepared using a minimum amount of NMP. The active mass of the sample was 10 mg. The paste was loaded onto the Ni-foam and kept in an oven at 75 °C overnight.

Supercapacitor experiments were carried out using the CorrTest Potentiostat instrument, which was used for the ORR study. Catalyst-loaded Ni-foam was used as the working electrode, Hg/HgO [saturated in 1 (M) KOH] was used as the reference electrode, and a Pt wire was used as the counter electrode. The experiments were performed using three different electrolytes: 1 (M) LiOH, 1 (M) NaOH, and 1 (M) KOH solutions.

3. Results and discussion

3.1. Materials characterization

3.1.1. Phase composition and XRD analysis. The phase composition and crystal structure of the as-prepared CCY composites were analyzed using powder X-ray diffraction (XRD). The XRD pattern (Fig. 2a) reveals three different

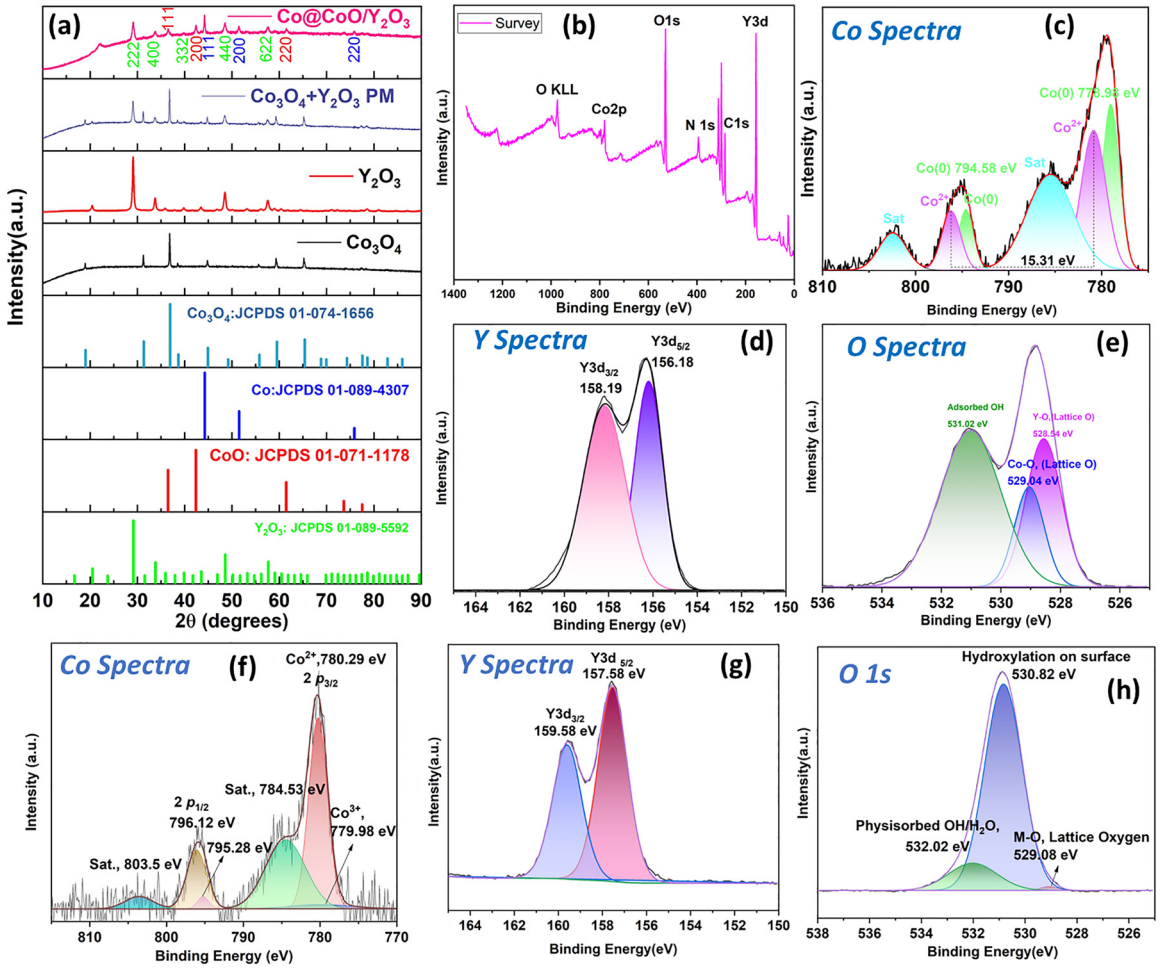

Fig. 2 (a) XRD analysis of the as-prepared composite and physical mixture of Co_3O_4 + Y_2O_3 PM (with stacked JCPDS data), (b)–(e) XPS survey of CCY, Co, Y, and O spectra with fitted curves, respectively, (f)–(h) post-cycling analysis of Co, Y and O spectra with fitting curves.

crystalline phases, that is, metallic cobalt (Co), cobalt(II) oxide (CoO), and yttrium(III) oxide (Y_2O_3), coexist. By comparing the diffraction peaks with standard JCPDS/PDF reference cards, the successful fabrication of the multi-phase hetero-structure was confirmed.

3.1.1.1. Y_2O_3 phase. The cubic Y_2O_3 phase (space group $Ia\bar{3}$, PDF no. 01-089-5592) is identified by characteristic diffraction peaks at 2θ = 20.51° (211), 29.17° (222), 33.81° (400), 35.92° (411), 39.87° (332), and 48.56° (440), with corresponding *d*-spacings of 4.32, 3.05, 2.64, 2.49, 2.25, and 1.87 Å, respectively.[36,37] The presence of multiple well-resolved reflections confirmed the crystalline nature of the Y_2O_3 phase.

3.1.1.2. Metallic Co phase. The characteristic peak of face-centered cubic (fcc) metallic cobalt (PDF no. 01-089-4307) appears at 2θ = 44.22° (111) with a *d*-spacing of 2.04 Å.[38,39] This peak is evidence for the presence of metallic Co cores and thus corresponds to the desired structure comprising core–shell-like Co@CoO.

3.1.1.3. CoO phase. The existence of a rock-salt structured CoO phase with the space group $Fm\bar{3}m$, PDF no. 01-071-1178 is indicated by the diffraction peaks at 2θ = 36.47° (111), 42.37° (200) and 61.52° (220) with *d*-spacings of 2.46, 2.13 and 1.51 Å respectively.[38,40] The presence of CoO reflections confirmed the oxidation of the cobalt surface, forming a shell around the metallic core.

3.1.1.4. Phase purity and heterostructure formation. No additional diffraction peaks corresponding to impurity phases (*e.g.*, Co_3O_4, Y–Co intermetallics, or unreacted precursors) were observed within the instrumental resolution, confirming the high purity of the synthesized materials. The relatively broad diffraction peaks indicate the nanoscale nature of crystallites. Application of the Scherrer equation to the major reflections yields average coherent domain sizes in the range of 21.8 to 85 nm (Average of 36.23) and lattice strain % (0.115 to 0.557) (calculation details provided in SI), which is favorable for electrocatalytic applications due to the high density of surface-active sites.[41,42] The coexistence of Co, CoO, and Y_2O_3 phases within a single composite suggests the formation of intimate heterointerfaces between these constituents. Such heterostructures are expected to facilitate synergistic electronic

interactions and charge redistribution, which can enhance electrocatalytic performance through optimized adsorption energies of reaction intermediates.[43,44]

3.1.2. XPS analysis. X-ray photoelectron spectroscopy (XPS) was performed to elucidate the surface chemical states and elemental composition of the CCY composite material. All binding energies were calibrated using the adventitious C 1s peak at 284.8 eV. The survey spectrum (Fig. 2b) confirms the presence of Co, Y, O, and C, consistent with the expected composition of the pyrolyzed complex-derived material. The high-resolution Co 2p spectrum (Fig. 2c) exhibited a doublet structure characteristic of cobalt species. The Co $2p_{3/2}$ region can be deconvoluted into two main components: a peak at ~778.98 eV attributed to metallic Co(0) and a higher binding energy component at ~780.5 eV assigned to Co^{2+} in CoO.[10,11] The Co $2p_{1/2}$ component appears near ~794.58 eV, giving a spin–orbit splitting of ~15.3 eV, consistent with the Co^{2+}/Co^{0} coexistence.[10,12] In addition, characteristic satellite features were observed at ~786 eV and ~803 eV, further supporting the presence of Co^{2} species (CoO) on the surface.[11,13] The simultaneous observation of metallic Co and CoO peaks validates the formation of a core–shell Co@CoO structure, consistent with the XRD results. The yttrium (Fig. 2d) 3d region was well resolved into the doublet Y $3d_{5/2}$ at 156.18 eV and Y $3d_{3/2}$ at 158.19 eV, consistent with Y^{3+} in yttrium oxide (Y_2O_3). These binding energies are characteristic of Y^{3+} in yttrium oxide (Y_2O_3), confirming that yttrium exists exclusively in the +3 oxidation state rather than as a metallic or lower valence species.[2,14] The O 1s spectrum (Fig. 2e) can be deconvoluted into three components: a low-binding-energy peak at ~528.6 eV attributable to lattice oxygen in Y-O (Y_2O_3),[2,15] a component at ~529.0 eV assigned to lattice oxygen in Co–O (CoO),[11,13] and a higher-binding-energy component at ~531.0 eV assigned to surface-adsorbed hydroxyl/water species.[16,17] The presence of both Y–O and Co–O lattice oxygen signals validates the formation of Y_2O_3 and CoO phases on the particle surface, while the adsorbed OH peak indicates surface hydroxylation, commonly observed for oxides exposed to air, and is often important for interfacial/catalytic behavior.[17,18]

The survey XPS spectrum shows additional features at ~1000 eV and ~400 eV, which are assigned to the O KLL Auger transition and N 1s signal,[45] respectively. The presence of trace nitrogen (~1.33 at%) is attributed to residual nitrogen-containing species originating from ligand decomposition and/or atmospheric adsorption. Raman spectra do not exhibit D and G bands, confirming the absence of graphitic carbon; thus, the detected nitrogen is not associated with N-doped carbon but rather with surface-bound species.

To assess the phase conversion after 10 000 cycles (post-cycling analysis), *ex situ* XPS analysis survey (Fig. S1) and core spectra (f–h) reveal that the Co 2p spectrum exhibits a well-defined spin–orbit doublet corresponding to the Co $2p_{3/2}$ and Co $2p_{1/2}$ components, Y spectra, and O 1s spectra. The Co 2p spectrum displays two characteristic spin–orbit doublets centered at ~780.4 and ~795.8 eV, corresponding to the Co $2p_{3/2}$ and Co $2p_{1/2}$ levels, respectively. The Co $2p_{3/2}$ peak can be deconvoluted into two components located at ~779.98 and ~780.29 eV, which are attributed to Co^{3+} and Co^{2+} species, respectively. This deconvolution confirms the coexistence of mixed-valence cobalt species, indicative of cobalt oxide phases. The Co $2p_{1/2}$ region can be deconvoluted into two contributions centered at ~795.28 and ~796.12 eV, which are attributed to Co^{3+} and Co^{2+} species, respectively. The spin–orbit splitting of ~15.1 eV between the Co $2p_{3/2}$ and Co $2p_{1/2}$ peaks is characteristic of cobalt oxide phases, particularly Co_3O_4 with a mixed-valence (Co^{2+}/Co^{3+}) state. Furthermore, the presence of prominent shake-up satellite peaks at ~784.53 eV and ~803.5 eV confirms the existence of Co^{2+} species and supports the formation of cobalt oxide.[46,47] Based on these observations, it can be inferred that the initial Co@CoO structure undergoes gradual transformation into a mixed-phase Co_3O_4 during prolonged cycling. This evolution can be rationalized by the formation of a CoOOH intermediate in the alkaline (KOH) electrolyte, which is commonly generated from Co or CoO under electrochemical conditions.[48] Over-extended cycling, this metastable CoOOH phase further converts into the thermodynamically stable spinel Co_3O_4 structure, leading to the observed phase transformation.[49,50] For the post cycling sample, yttrium (Y $3d_{5/2}$) spectra little bit shifted to higher binding energy (Y$3d_{5/2}$: 157.58 eV, Y$3d_{3/2}$: 159.58 eV) compared to virgin materials (Y$3d_{5/2}$: 156.18 eV, Y$3d_{3/2}$: 158.19 eV), which may be due to oxidation of the cobalt to higher oxidation state (Co^{3+}), pulling electron density away from yttrium through the bridging oxygen atoms. Electron withdrawal enhances the effective nuclear charge on yttrium atoms, strengthening the interaction with core electrons and leading to a shift of the XPS peaks toward higher binding energies.[51] The oxygen spectrum fitting also reveals the presence of three different components in the sample, a maximum amount of surface hydroxyl groups (530.82 eV), consistent with the formation of the CoOOH-like phase during alkaline cycling, also the presence of metal–O lattice bonds (529.08 eV) and physisorbed water or the hydroxyl group (532.02 eV).[52] The largest area indicates that the 10 000 cycles successfully transformed the surface into a highly hydroxylated species, a defect-rich environment, which is ideal for high capacitance retention.[53,54]

3.1.3. Raman spectroscopy analysis. Raman spectroscopy was also used to supplement the XRD and XPS measurements for investigating lattice vibrational features and local structural disorders in the CCY composite. As shown in Fig. 3, the Raman spectrum shows characteristic vibrational features related to CoO and Y_2O_3, along with an additional high-frequency band that can be attributed to interfacial or defect-related effects.

Raman bands at around 192, 481, 516, and 678 cm^{-1} can be assigned to those previously defined vibrational modes of rock-salt CoO.[55] Although ideal bulk CoO is Raman inactive due to its centrosymmetric crystal structure, these modes are commonly detected in nanocrystalline or defect-rich CoO and are attributed to disorder-activated optical and acoustic phonons. The appearance of these bands is consistent with the CoO phase identified by XRD and the presence of Co^{2+} species confirmed by XPS, further supporting the formation of a surface-

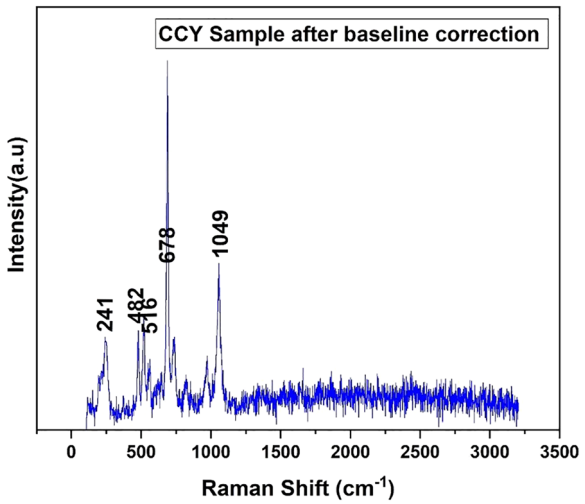

Fig. 3 Raman analysis as a prepared catalyst.

oxidized CoO shell in the Co@CoO architecture. Two additional Raman peaks located at ~376 and ~551 cm^{-1} can be assigned to Raman-active modes of cubic Y_2O_3 with a bixbyite structure, originating from Y–O lattice vibrations.[56,57] These observations are in good agreement with the XRD identification of crystalline Y_2O_3 and the exclusive presence of Y^{3+} species revealed by the Y 3d XPS spectrum, confirming the structural and chemical integrity of the Y_2O_3 phase. Notably, a weak but distinct Raman feature appeared at ~1049 cm^{-1}, which could not be assigned to the intrinsic vibrational modes of either CoO or Y_2O_3.[16] This band is therefore tentatively attributed to a second-order or defect-activated metal–oxygen vibrational mode associated with interfacial coupling between the CoO and Y_2O_3 phases. The emergence of such high-frequency features has been reported in mixed-metal oxide heterostructures and is commonly linked to local lattice distortion, symmetry breaking at heterointerfaces, and oxygen-vacancy-related defects.[11,16,58] Importantly, this feature does not correspond to the D or G bands of carbonaceous species (~1350 and ~1580 cm^{-1}), nor to the reported vibrational modes of cobalt or yttrium nitrides, excluding contributions from unintended phases. Taken in conjunction with the XRD evidence of multiphase coexistence and XPS identification of mixed oxidation states and surface hydroxylation, the Raman data offer corroborative evidence for defect-rich oxide heterointerfaces in the CCY composite. These interfacial structures are beneficial for interfacial charge redistribution and surface reaction kinetics in electrocatalysis.[10,11,16,58]

The textural characteristics of the CCY were determined by N_2-adsorption–desorption isotherms at 77 K (Fig. 4a), which showed the isotherm to be a characteristic Type IV(a) with an H3 hysteresis loop according to the IUPAC classification and indicated a mesoporous nature derived from agglomerated nanoparticles.[59] The H3 hysteresis loop is generally linked to slit-shaped pores and interparticle voids, which in this system can be ascribed to the arrangement of Co@CoO and Y_2O_3 nanoparticles. This finding aligns with the multiphase heterostructure detected by XRD and the defect-rich oxide interfaces revealed by XPS and Raman spectroscopy.[59,60] When the relative pressures are low ($P/P_0 < 0.2$), nitrogen is adsorbed as a monolayer on the oxide surfaces, followed by multilayer adsorption at intermediate pressures (P/P_0 = 0.2–0.6). The significant hysteresis detected at higher relative pressures ($P/P_0 > 0.6$) was due to capillary condensation within the mesopores. The steep rise in adsorption at $P/P_0 \rightarrow 1$ is attributed to larger mesopores and interparticle macropores formed by nanoparticle aggregation.[60,61] Table 1 summarizes the quantitative textural parameters derived from the BET and BJH analyses (Fig. S2).

The achieved hierarchical mesoporous structure features pores mainly at 7–20 nm coupled with larger interparticle voids, which is beneficial for electrocatalytic applications. Such a structure promotes fast mass transportation of reactants (O_2, OH^-) and electrolyte ions to the active sites while maintaining structural integrity. When combined with the defect-rich CoO–Y_2O_3 heterointerfaces identified by Raman and XPS analyses, these textural features are expected to contribute for improving electrocatalytic performance.[60,62]

3.1.4. Morphology and elemental distribution (FESEM-EDX, HRTEM). Morphological characterization was performed using field-emission scanning electron microscopy (FESEM) (Fig. 4b–d), energy-dispersive X-ray spectroscopy (EDX) analysis, and elemental mapping (Fig. S3). From the study, it has been observed that cocoon like CoO oxide formed on the surface of Y_2O_3. Elemental color mapping also supports the formation of the composite. The EDX analysis supports the presence of Co, Y, O, and N. The presence of nitrogen may be ascribed to trapped nitrogen/chemisorbed/physisorbed nitrogen, which does not have a stable, long-range crystalline structure (no XRD peaks) and lacks a covalent bond directly to the metal or carbon matrix that would appear in Raman spectra, only appearing in EDX analysis. High-resolution TEM (HRTEM) images of the virgin Co@CoO–Y_2O_3 sample clearly reveal a well-defined core–shell heterostructure (Fig. 4g–i). The particles exhibit an oval-like morphology with a distinct contrast difference between the dense metallic core and the other oxides are surrounded (CoO) and attached(Y_2O_3) to it. The HRTEM analysis of the virgin sample reveals the formation of a heterostructure zone: the planes of Co (111, 2.04 Å), CoO (111, 2.4 Å), and Y_2O_3 (222, 3.06 Å) formed a heterostructure zone, which might be responsible for the excellent catalytic activity. Post-cycling HRTEM analysis of the electrode is inherently challenging, as the recovered material is mixed with binders and conductive additives during ink preparation, making it difficult to unambiguously resolve phase transformations at the nanoscale. Hence, the post-cycling *ex situ* XPS spectroscopy is conducted to support the phase change.

4. Electrochemical characterization

4.1. Electrocatalytic reduction of molecular oxygen, *i.e.* oxygen reduction reaction (ORR) reaction

The performance of the electrocatalytic reduction of oxygen was estimated using different electrochemical techniques, such as

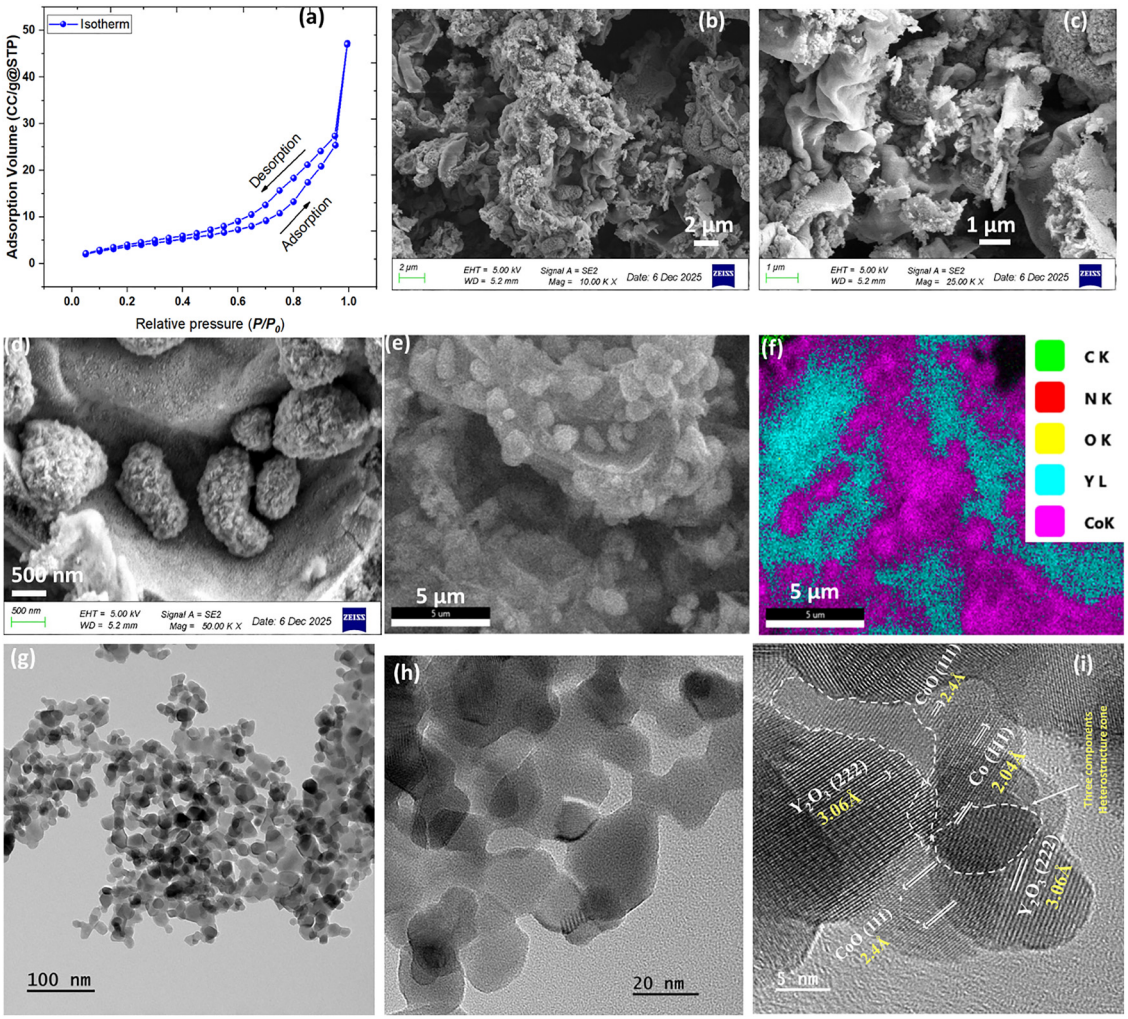

Fig. 4 (a) BET analysis of the CCY sample, (b)–(d) FESEM images of the CCY sample at different magnifications, and (e) and (f) selected sample area with elemental color mapping, (g)–(i) HRTEM images in different magnifications, showing the formation of the heterostructure boundary/zone of Co, CoO, and Y_2O_3.

Table 1 The results obtained from BET analysis

BJH desorption summary				
Sample	Average pore size (diameter)	Surface area	Desorption pore diameter (nm)	Desorption pore volume
Co@CoO–Y_2O_3	19.6442 nm	20.091 $m^2\ g^{-1}$	7.773 nm	0.074 cc g^{-1}

cyclic voltammetry (CV), linear sweep voltammetry (LSV), and electrochemical impedance spectroscopy (EIS), in a three-electrode setup in an aqueous 1 M KOH electrolyte at room temperature (RT). The selection of KOH molarity (1 M) also plays a role because it provides excellent electrochemical performance for the electrodes. Graphite and Hg/HgO electrodes were used as the counter and reference electrodes, respectively. The ORR catalytic activity of the prepared CCY catalyst was systematically evaluated and compared with that of the state-of-the-art benchmark Pt/C (20%) under identical conditions. The prepared catalyst shows a well-defined cathodic reduction peak at ~−0.4 V in O_2-saturated electrolyte, whereas no such peak is observed in N_2 saturated electrolyte (Fig. 5a and Fig. S4), indicating that the CCY catalyst is well capable of the electrochemical reduction of molecular O_2 occurs at the catalyst surface (Fig. 5a). The LSV curve exhibited a characteristic S-shaped profile, in which the catalytic current increased with the applied potential and eventually reached a plateau, commonly referred to as the limiting current. This plateau arises from the transition from charge-transfer-controlled kinetics to mass-transport-controlled behavior, where the overall reaction rate is governed by the diffusion of the reactant to the electrode surface. Under these conditions, the catalyst operates at its mass-transport-limited rate, consuming the available reactants within the diffusion layer.[63]

In the conventional mechanism of the ORR in alkaline media, molecular oxygen can undergo either a direct four-electron pathway or a two-electron pathway involving peroxide intermediates. To reveal the ORR kinetics and reaction pathway, RRDE measurements were performed at various rotation

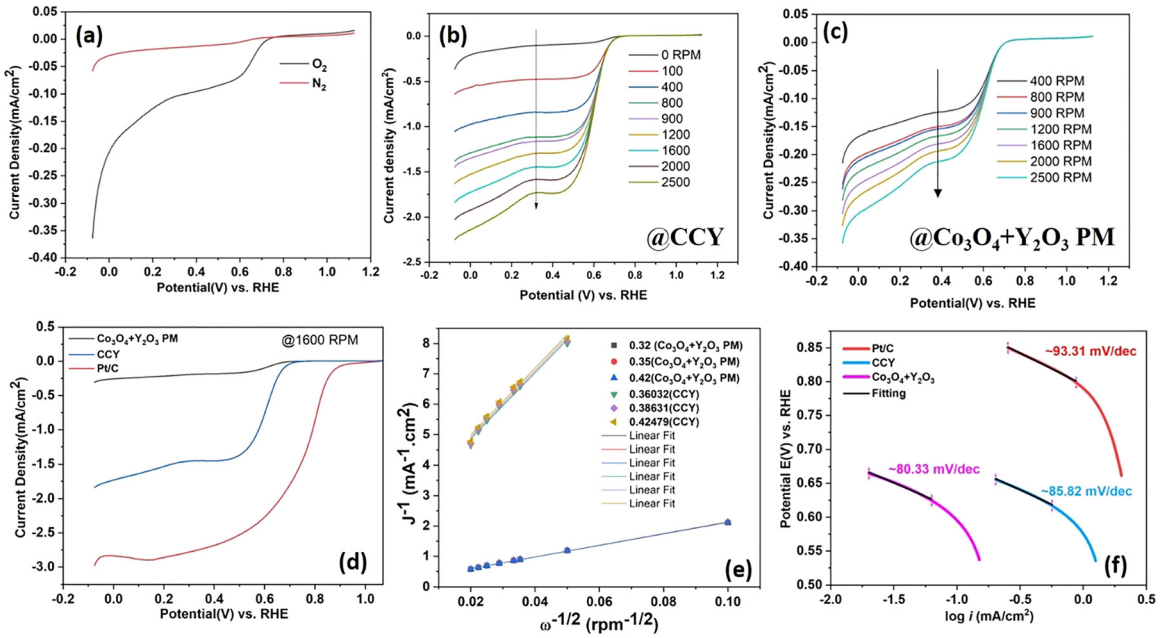

Fig. 5 (a) LSV of CCY in the presence O_2 and N_2 at 0 rpm, (b) and (c) LSV curves of the CCY and Co_3O_4 + Y_2O_3 PM sample at different rotation speeds from 0 to 2500 rpm, (d) comparison of LSV plots for the Co_3O_4 + Y_2O_3 PM, sample CCY, and Pt/C at 1600 RPM, (e) Koutecky–Levich (KL) plots of Co_3O_4 + Y_2O_3 PM, sample CCY, (f) Co_3O_4 + Y_2O_3 PM, sample CCY, and Pt/C at 1600 rpm.

speeds between 0 and 2500 rpm (Fig. 5b). The gradual rise in the limiting current density as a function of the rotation speed indicates increased oxygen mass transport and confirms diffusion-controlled behavior at lower potentials.

All potentials were converted to the reversible hydrogen electrode (RHE) scale using the following relation:

$$E_{vs.\ RHE} = E_{vs.\ Hg/HgO} + 0.098 + 0.059 \times pH \quad (1)$$

The LSV curves can be divided into three distinct regions: (i) a kinetically controlled region, which is generally above the potential of 0.79 V *vs.* RHE in the present study; (ii) a mixed kinetic–diffusion region between 0.79 and 0.42 V *vs.* RHE; and (iii) a diffusion-limited region at low potentials below 0.42 V *vs.* RHE. The merit of an electrocatalyst depends on the difference in the half-wave potential ($\Delta E_{1/2}$) between the catalyst and Pt/C. In the present study, the CCY catalyst-modified electrode showed a minimum $\Delta E_{1/2}$ value (0.603 V *vs.* RHE) compared to Co_3O_4–Y_2O_3 PM (0.60 V *vs.* RHE) and Pt/C (0.807 V *vs.* RHE). The half-wave potential of the CCY catalyst and Co_3O_4–Y_2O_3 PM is comparable, which means overall catalytic activity and density of accessible active sites are almost similar for both, but less than Pt/C.[64] These results are consistent with previously reported literature values for analogous transition metal oxide-based ORR catalysts, and a detailed comparison with literature reports is provided in Table S1.

The diffusion-limiting current density of the CCY electrode increased with an increase in the RRDE rotation speed, which was attributed to the faster diffusion of O_2 molecules onto the electrode surface at a higher rotation speed. Furthermore, Koutecky–Levich (K–L) equation analysis was performed to determine the electron transfer number (n) using the following relation:

$$\frac{1}{J} = \frac{1}{J_L} + \frac{1}{J_K} = \frac{1}{B\omega^{\frac{1}{2}}} + \frac{1}{J_K} \quad (2)$$

where J, J_L, and J_k represent the experimentally measured current density, diffusion-limiting current density, and kinetic-limiting current density, respectively, and ω denotes the angular rotation speed of the rotating disk electrode. The parameter B was determined from the slope of the K–L plots (J^{-1} *vs.* $\omega^{-1/2}$) according to the Levich equation, as given below.

$$B = 0.2nFC(O_2)D(O_2)^{2/3}\upsilon^{-1/6} \quad (3)$$

Here, 0.2 is used because the rotation is expressed in rpm. 'n' is the number of electrons involved in the reaction, 'F' is the Faraday constant, $C_{(O_2)}$ is the bulk oxygen concentration, 'D_{O_2}' is the diffusion coefficient of oxygen in 1 (M) KOH, and υ is the kinematic viscosity of the electrolyte. The K–L plots (Fig. 5e) exhibit good linearity and near-parallel slopes over a range of potentials, indicating first-order reaction kinetics with respect to the dissolved oxygen. The electron transfer number calculated from the K–L slopes was approximately n = 2.17, suggesting that the ORR on CCY predominantly proceeds *via* a two-electron pathway, leading to peroxide (HO_2^-/H_2O_2) formation in alkaline media. In alkaline medium, the $2e^-$ ORR process leads to the formation of hydroperoxide species (HO_2^-), which then transform into hydrogen peroxide. It is also worth noting that the electrochemical production of H_2O_2 is more cost-effective and environmentally benign than the conventional anthraquinone method. Because of the potential benefits in cost and production safety, the electrochemical process for the formation of H_2O_2 is garnering more attention.[65] In the present

work, the Co@CoO/Y_2O_3 heterostructure promotes a preferential 2e$^-$ transfer pathway, which can be attributed to interfacial electronic interactions between Co/CoO and Y_2O_3. This heterointerface likely modulates the adsorption energy of oxygenated intermediates and stabilizes the *OOH species, thereby suppressing O–O bond cleavage and favoring H_2O_2 formation. Additionally, the heterostructure interface facilitates efficient charge transfer and provides abundant active sites for O_2 adsorption and activation. Despite following a 2e$^-$ pathway, the catalyst exhibits a favourable onset potential, reasonable current density, and good stability. These results suggest that the designed CCY catalyst is a promising candidate for selective H_2O_2 production *via* the ORR.

The peroxide yield was estimated using the rotating ring-disk electrode (RRDE) formalism:[66,67]

$$n = \frac{4I_d N}{I_d + I_r} \quad (4)$$

where N is the collection efficiency (N), and I_d and I_r are the disk and ring currents, respectively. From an earlier study, we know that if n = 2, then $I_r = I_d N$. Now, we can calculate the %H_2O_2 formation:

$$\%H_2O_2 = 100\frac{nI_r}{I_d N} = 100\frac{2I_r}{I_d N + I_r} = 100\frac{4-n}{2} \quad (5)$$

Based on the experimentally derived n value, the CCY catalyst exhibited nearly 100% H_2O_2 selectivity, consistent with the dominant two-electron ORR pathway.

Furthermore, the stability of the catalyst was measured by chronoamperometry, in which the catalyst maintained a current density of ~0.8 mA cm^{-2} for 24 h (Fig. S5) and the catalyst did not show any major decline in the current density even after 24 h of the stability test.[68] Another comparison was drawn between the CCY catalyst and Pt/C to determine the diffusion-limited current density of both catalysts. Hence, the LSV polarization curve was obtained at 1600 rpm with a scan rate of 5 mV s^{-1} for the catalyst and commercial Pt. The Co@CoO–Y_2O_3 material delivers a diffusion-limited current density comparable to that of Pt, highlighting its strong mass transport and reduction capability in the oxygen reduction reaction (ORR), although it exhibits a slightly lower negative onset potential (790 mV) relative to Pt (909 mV) under the same conditions. This behavior is consistent with previous reports on Co-based and Co/CoO-derived ORR catalysts, which demonstrated limiting current densities similar to that of Pt/C. Although these catalysts often exhibit slightly lower onset or half-wave potentials, this is attributed to variations in the intrinsic activity and surface binding energetics of oxygen intermediates on non-precious surfaces.[69,70] Tafel analysis (Fig. 5f) reveals a slope of 85.82 mV dec^{-1} for CCY, which is lower than that of Pt/C (93.31 mV dec^{-1}), indicating comparatively faster ORR kinetics. This observation suggests improved charge-transfer characteristics in the CCY catalyst, although its overall activity remains lower than that of Pt/C, as reflected in the half-wave potential. A similar trend in Tafel slopes for transition metal oxide-based ORR catalysts has been reported in the literature.[71] Despite this, the sustained diffusion-limited current density and high peroxide selectivity confirm that Co@CoO–Y_2O_3 serves as a stable and effective non-noble-metal electrocatalyst for the two-electron ORR pathway in alkaline environments. Although the physical mixture exhibits a slightly higher electrochemical activity than CCY, the latter delivers nearly eight times higher current density (PM: 0.18 mA cm^{-2}, CCY: 1.44 mA cm^{-2}). Since current density directly reflects the rate of electrochemical reactions per unit electrode area, this substantial increase indicates that, for each square centimetre, CCY facilitates a much higher rate of oxygen reduction compared to the Co_3O_4 + Y_2O_3 physical mixture. This clearly demonstrates that CCY possesses superior intrinsic reaction kinetics and more efficient catalytic activity.

4.2. Supercapacitor performance of CCY in different alkali electrolyte media

In addition to its ORR activity, the CCY composite was further explored as a battery-type supercapacitor electrode. As the choice of electrolyte is a crucial factor in determining the charge transport, reaction kinetics, and overall device performance, the electrochemical behavior of CCY was examined in three different electrolytes, namely KOH, NaOH, and LiOH, using the Hg/HgO reference electrode. As in aqueous systems the potential window cannot reach above 1 V;[72] therefore, the potential window was carefully optimized (Fig. S6a and b) within the region where the current response changes nearly linearly with the applied potential (0–0.55 V), while excluding the region exhibiting abrupt current variations that may arise from undesirable electrochemical reactions or non-capacitive processes. The cyclic voltammetry (CV) curves were recorded within the potential range of 0 to 0.55 V, showing two distinct peaks, which were the reduction and oxidation peaks of cobalt. The peak at 0.40 V *vs.* HgO/Hg for oxidation (anodic sweep, sweeping towards a more positive potential) and 0.253 V *vs.* HgO/Hg for reduction (cathodic sweep, sweeping towards a more negative potential) corresponded to the CoO nanoparticles. The well-defined redox peaks in the redox process govern the faradaic-type charge storage mechanism of the CCY electrode in the electrolyte solution. These peaks are also related to the redox couple of the Co^{2+}/Co^{3+} (Co–O/Co–O–OH) pair associated with HO^-, confirming the typical battery-type behavior of the electrode. In addition, among the three electrolytes, the CCY electrode exhibited a larger CV integral area and the highest anodic and cathodic peak currents in KOH compared to NaOH and LiOH electrolytes, indicating its superior charge storage properties. This behavior can be ascribed to the smaller hydrated radius (~3.3 Å, Table 2) and higher ionic conductivity of K^+ ions, which facilitate faster ion diffusion and more efficient penetration into the porous electrode matrix. In contrast, the NaOH and LiOH electrolytes showed relatively lower current responses, with LiOH exhibiting the smallest CV area owing to the sluggish transport kinetics of strongly solvated Li^+ ions (~3.8–4.0 Å).

Furthermore, the quasi-symmetrical shape of the CV curves and minimal peak shift further indicate the good

Table 2 List of radii of Li^+, Na^+ and K^+ [73,74]

Ion	Ionic radius (Å)	Hydrated radius (Å)
Li^+	~0.76	~3.8–4.0
Na^+	~1.02	~3.6
K^+	~1.38	~3.3

electrochemical reversibility and structural stability of the Co@CoO–Y_2O_3 composite in alkaline media.

The charge storage process in alkaline media can be described by the following reversible redox reactions:

$$CoO + HO^- \leftrightarrow CoOOH + e^-$$

$$CoOOH + HO^- \leftrightarrow CoO_2 + H_2O + e^-$$

These reactions involve proton-coupled electron transfer (PCET), in which hydroxide ions act as both charge carriers and reactants. The presence of metallic Co (Co^0) further improves the electrical conductivity, facilitating rapid electron transfer between the redox-active CoO sites. The presence of Y_2O_3 does not participate in the reaction; it only helps to adsorb the HO^- ion as it provides oxygen vacancy sites and affects the possible Co–O–Y bridge center, preventing Co dissolution. It also stabilizes the peak position and minimizes peak broadening.

The electrochemical surface area (ECSA) (Fig. S6e) is also estimated from the double-layer capacitance using ECSA = C_{dl}/C_s, where C_s is typically taken as 0.04 mF cm^{-2} in alkaline electrolyte (Fig. S6f). A higher C_{dl} reflects a larger electrochemically accessible surface area and thus a greater density of exposed catalytic sites. The correlation between C_{dl} and ECSA has been widely used to evaluate metal oxide and carbon-based electrocatalysts. The catalyst exhibits a BET surface area of 20.09 $m^2\ g^{-1}$, while the electrochemically active surface area (ECSA) estimated from CV measurements corresponds to ~10.5 $m^2\ g^{-1}$. This suggests that nearly 52% of the physical surface area is electrochemically accessible to the electrolyte. The double-layer capacitance (C_{dl}) normalized per mass is ~4.2 F g^{-1}, corresponding to ~0.4 F m^{-2}, which is consistent with the typical capacitance values reported for metal oxide electrocatalysts. The good agreement between ECSA and C_{dl} further confirms that the observed capacitive response arises predominantly from the electrochemically accessible surface sites. Here, it is important to note that BET and ECSA probe different aspects: BET measures total gas-accessible surface area, while ECSA reflects only the electrolyte-accessible and electrochemically active sites. Therefore, ECSA values lower than BET is expected. Similar discrepancies have been reported in the literature; for example, Burrow *et al.* reported a high BET surface area (~96 $m^2\ g^{-1}$) but a comparatively low ECSA (~7.5 cm^2), highlighting that not all physical surface area contributes to electrochemical activity.[75]

The galvanostatic charge–discharge (GCD) profiles for the CCY electrode are depicted in Fig. 6b, recorded at a current density of 0.5 A g^{-1} using three different alkaline electrolytes. All the GCD curves exhibited nonlinear charge–discharge characteristics with a plateau, confirming the dominant pseudocapacitive nature and signature curve of the battery-type behavior. The GCD curve tested in the KOH electrolyte delivered the longest discharge time, which was directly correlated with its specific capacity. The enhanced performance in KOH can be ascribed to the lower internal resistance and ease of accessing pores or accessing a larger surface area. In contrast, NaOH exhibited a moderate discharge time, and LiOH exhibited the

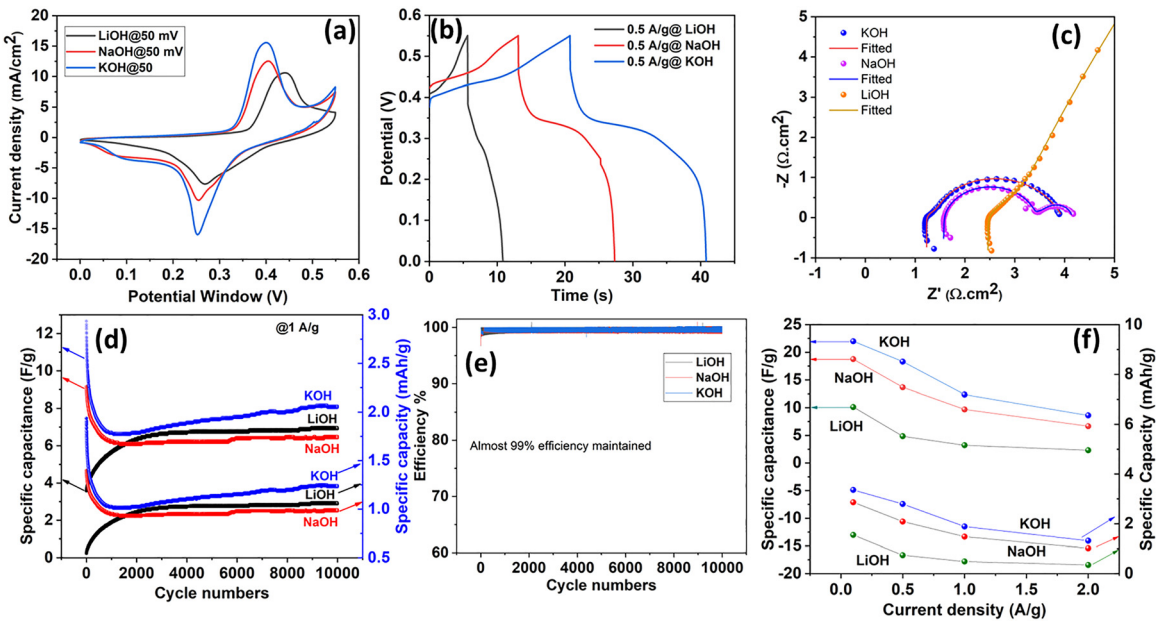

Fig. 6 (a) CV comparison in different electrolytes at 50 mV s^{-1}, (b) GCD at a constant current density of 0.5 A g^{-1}, (c) EIS plots of the CCY sample in different electrolytes (the same *x* and *y* axis scale), (d) cyclic stability test (10 000 cycles) of the CCY sample, (e) CCY sample maintained almost 99% efficiency during the stability test, (f) Sp. capacitance, sp. capacity *vs.* current densities for different electrolytes used in the test.

lowest discharge time, reflecting the limited electrochemical utilization of the active sites. The minimal IR drop was also observed during the starting process, particularly in KOH, indicating a low equivalent series resistance (ESR) and efficient electrode–electrolyte contact. All the electrochemical impedance spectroscopy (EIS) tests of the CCY electrode were carried out by applying an ac amplitude of 0.55 V in three different electrolytes (KOH, NaOH, and LiOH) within the frequency range of 0.1–10^5 Hz. The electrode exhibited a prominent semicircular arc in KOH and NaOH, indicating charge transfer resistance. All spectra consist of a depressed semicircle in the high-frequency region, followed by an inclined line in the low-frequency region, characteristic of the charge-transfer resistance (R_{ct}) and diffusion-controlled Warburg impedance, respectively. The EIS curves were fitted with a suitable circuit diagram (Fig. S7), and several parameters were extracted to explore the mechanism of charge transfer in these electrodes. After fitting the circuit, the data show that the R_{ct} values in KOH, NaOH, and LiOH are 0.630, 1.8713, and 3.071 Ω, respectively. The data suggest that the lower charge transfer resistance experienced in KOH (the lowest value) facilitates the ion insertion/de-insertion process.[76] In impedance spectroscopy, the resistor acts as the equivalent series resistance, and the capacitor is related to the capacitance. The net impedance can be expressed through the following equation, where $\omega = 2\pi f$ and f is the frequency in Hz.[76]

$$Z_{RC} = R + 1/j\omega C \quad (6)$$

From the above equation, it can be expressed that at higher frequencies, the dominant term is ESR, while at lower frequency values, the capacitive term is effective, and the system acts like a pure capacitor. The EIS after 10 000 cycles also showed changes in solution resistance (1.5931 Ω cm^2) and charge transfer resistance (R_{ct}) (3.8046 Ω cm^2) due to reversibility loss and possible structural deformation, resulting in degraded performance (Fig. S7d).

Long-term cycling stability was evaluated over 10 000 charge–discharge cycles at 1 A g^{-1} (Fig. 6d). In KOH and NaOH electrolytes, the electrode exhibited an initial decrease in specific capacitance during the early cycles, which was attributed to progressive electrolyte infiltration and gradual exposure of electroactive sites. Notably, the electrode in KOH maintained the highest specific capacity throughout the cycling test, followed by those in LiOH and NaOH. After prolonged cycling, negligible capacity fading was observed, highlighting the excellent structural integrity and electrochemical robustness of the composite. The presence of Y_2O_3 likely contributes to enhanced structural stabilization and the suppression of cobalt dissolution during repeated redox cycling. Interestingly, distinct early cycle trends were observed depending on the electrolyte used. In KOH and NaOH electrolytes, the specific capacitance exhibited a slight initial decrease. The initial decrease in capacitance, followed by gradual recovery and stabilization, can be attributed to an electrochemical activation process accompanied by the redistribution of the initially trapped ionic species at the solid–electrolyte interface. During the early cycling stages, these trapped ions undergo progressive reorganization and migration toward energetically more favorable adsorption and redox-active sites, which enhances electrolyte accessibility and improves the charge transfer efficiency. Consequently, a more electrochemically active and stable interface was established, leading to enhanced and stabilized charge storage performance upon continued cycling.[77] In the case of LiOH, the specific capacitance started from low to high can be attributed to sluggish Li^+ transport and strong solvation effects that delay full utilization of redox-active sites. Continued cycling and electrolyte penetration enable full access to redox-active sites, resulting in a gradual increase in the specific capacitance.

The detailed electrochemical reaction kinetics of the as-synthesized electrodes were investigated to confirm the diffusion-controlled kinetic characteristics using CV profiles. The CV curves of the electrode largely retained their characteristic shapes in all three electrolytes as the scan rate increased from low to high values, indicating excellent rate capability and good structural integrity under rapid potential sweeping. Fig. 7d–f shows the relationship between the square root of the scan rate and the corresponding anodic and cathodic peak currents for the CCY electrode. In all cases, the peak currents increased linearly with the square root of the scan rate, confirming that the electrochemical reactions were predominantly governed by diffusion-controlled faradaic processes, which are characteristic of battery-type charge storage behavior.

To further elucidate the underlying charge-storage mechanism, the reaction kinetics of the electrode were quantitatively analyzed by separating the diffusion-controlled and capacitive-controlled contributions in three different electrolytes. The analysis employs the power–law relationship between peak current and scan rate, expressed by the following equation: $i = a\nu^b$. The contributions of capacitive-controlled and diffusion-controlled processes were quantified by correlating the peak current (i) of the CV curves with the scan rate (ν) according to the power-law relationship:[78]

$$\log(i) = \log a + b\log(\nu) \quad (7)$$

where a and b are the adjustable parameters. Various electrochemical processes can be identified depending on the b values. If b is ∼ 0.5, the process indicates diffusion-controlled battery-type behavior, whereas if b is ∼0.5–1.0 is a combination of diffusion and surface-controlled processes. In this study, the b value was obtained as ∼close to 0.5 for all the electrolytes, indicating that the process is a diffusion-controlled faradaic charge storage process, which is typical of battery-type behavior.[79,80] The charge storage behavior was quantitatively assessed following the method proposed by Dunn, where the total current at a specific potential is expressed as the sum of capacitive ($\propto \nu$) and diffusion-controlled faradaic ($\propto \nu^{1/2}$) components, as given in Eqn 8.[78] The sum of the surface ($k_1\nu$) and diffusion-controlled ($k_2\nu^{1/2}$) processes can be represented as the total current density in the CV profile at constant potential (V), as demonstrated by the following equations:

$$i(V) = k_1\nu + k_2\nu^{1/2} \quad (8)$$

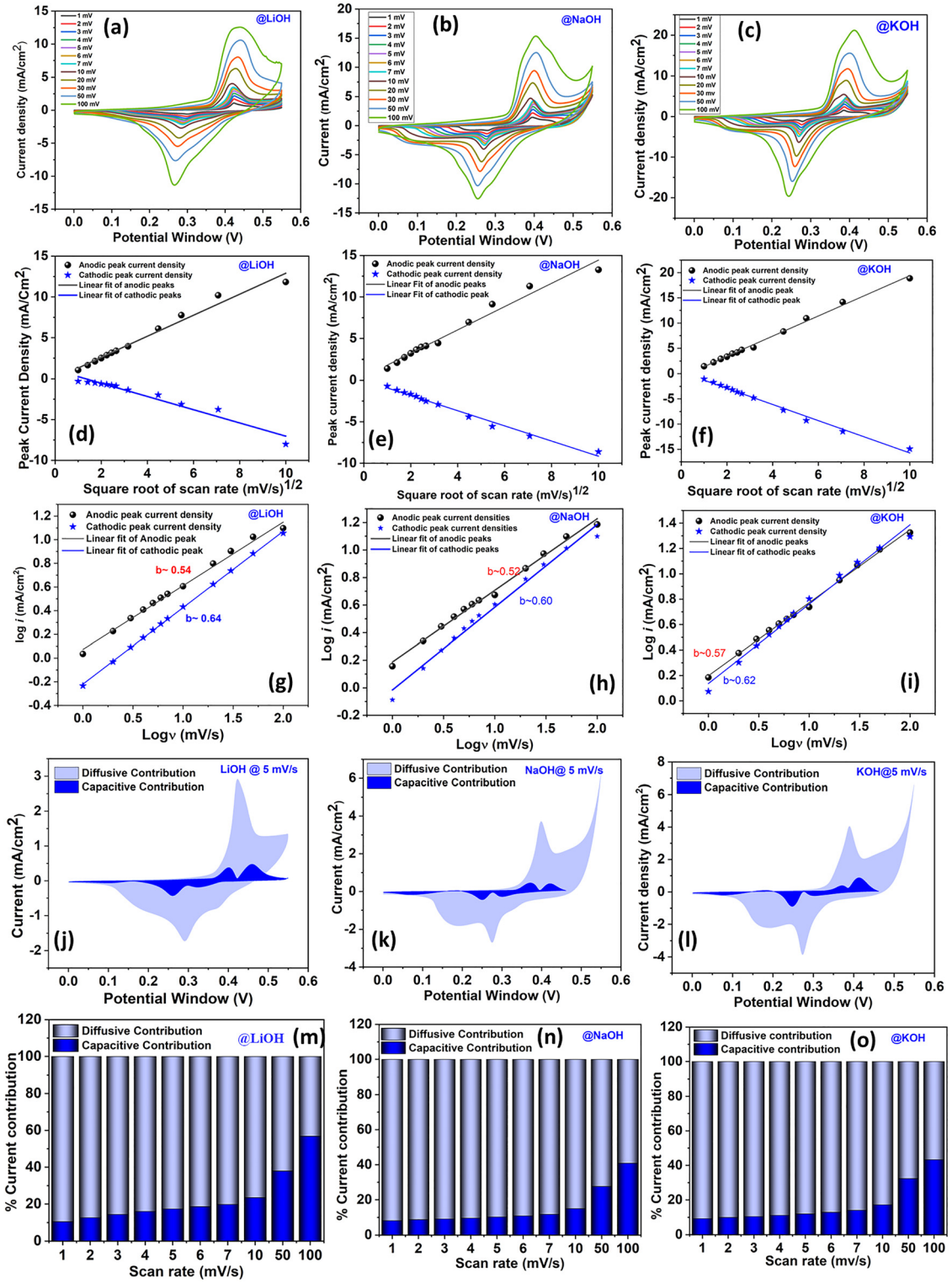

Fig. 7 (a)–(c) CV curves at different scan rates, (d)–(f) current density *vs.* square root of the scan rate, (g)–(i) log(*i*) *vs.* log(*ν*) plots, (j)–(l) percentage of current contribution plots, and (m)–(o) areal current contribution of CV curves at a scan rate of 5 mV s^{-1} in LiOH, NaOH, and KOH, respectively.

Therefore, a plot of $i(V)/\nu^{1/2}$ *vs.* $\nu^{1/2}$ would be a straight line as follows:

$$i(V)/\nu^{1/2} = k_1\nu + k_2 \quad (9)$$

where k_1 and k_2 are obtained from the slope and intercept of the linear fit of eqn (9), respectively. Fig. 7(g–i) presents the plot of $i(V)/\nu^{1/2}$ *vs.* $\nu^{1/2}$ of three electrodes based on the above equations.

The ratio of surface-controlled capacitive to diffusion-controlled battery-type processes was calculated and is presented in Fig. 7(j–o). From the figure, it can be observed that the diffusion-controlled process at a scan rate of 10 mV s^{-1} (LiOH: 76.54%, NaOH: 85.10918%, KOH: 82.83814%) decreased ten times faster at a scan rate of 100 mV s^{-1} (LiOH: 43.21%, NaOH: 59.16%, KOH: 56.73%). These results show that the charge storage mechanism in these three electrolytes is mainly diffusion-controlled. Fig. 7(m–o) shows the areal capacitance of CCY in different electrolytes at a scan rate of 5 mV s^{-1}. For all three electrolytes, the area of the diffusion-controlled contribution was significantly higher than that of the capacitive-controlled process. The battery-type (diffusion-controlled) behavior is the dominant mechanism for the CCY electrodes. The unique morphology of the electrodes with a mesoporous surface, having relatively larger voids within the nanostructure, facilitates the accumulation/intercalation of charges at the inner electroactive sites, contributing to the dominant battery-type diffusion capacitance. The minor contribution from the surface-controlled process originates partly from the following: (i) surface pseudocapacitance (manifested by the reversible adsorption/desorption of metal ions (Li^+, Na^+, and K^+) on the CCY surfaces, accompanied by the valence conversion of Co^{2+}/Co^{3+} or Co^{4+} in an aqueous electrolyte) due to the presence of abundant redox-active surface sites at the CCY; (ii) electric double-layer capacitance (EDLC) at the nanostructure (that provides a very high specific surface area for a non-faradaic charge storage process). The CCY electrode exhibited a slightly lower diffusion-controlled contribution in LiOH than in NaOH and KOH, mainly due to the presence of a larger hydrated structure, which contributed to the minor capacitive-controlled processes. The specific capacity was plotted as a function of the corresponding current density, as shown in Fig. 6f. The specific capacitance and specific capacity were calculated using the following equations:

$$C_s = \frac{I\Delta t}{\Delta V \times m} \left(\mathrm{F\ g^{-1}}\right) \tag{10}$$

$$C_s = \frac{I\Delta t}{m \times 3.6} \left(\mathrm{mAh\ g^{-1}}\right) \tag{11}$$

The electrode exhibited specific capacities of KOH: 22 F g^{-1} (3.36 mAh g^{-1}), NaOH:18.74 F g^{-1} (2.86 mAh g^{-1}), and LiOH: 10.12 F g^{-1} (1.54 mAh g^{-1}) at 0.1 A g^{-1}. The sluggish kinetics and substantial resistance at higher current densities caused the specific capacity to decrease as the current density increased. The capacitance values reported in this study represent gravimetric capacitance (10 mg of active mass), calculated using the active mass of the electrode material. The specific capacitance was determined without applying any iR correction.

At a current density of 1 A g^{-1}, the cycling performance of the hybrid device was investigated for 10 000 cycles, as shown in Fig. 6d. The device showed excellent cycling stability after 10 000 cycles with a capacitance retention of 64.14% in KOH, 70.71% in NaOH, and 193% in LiOH. Such values exceeding 100% have been occasionally reported in the literature and are generally attributed to factors such as progressive activation of electroactive sites, structural optimization leading to improved ion transport, and enhanced electrolyte wetting and ion accessibility during cycling, rather than a true physical increase in capacitance. Similar observations have been reported in previous studies.[81–85]

Furthermore, we studied the coulombic efficiency (η) of the fabricated device by using the following equation:

$$\eta = \frac{t_d}{t_c} \times 100\% \tag{12}$$

where t_d and t_c are the discharging and charging times (s), respectively. The coulombic efficiency of the CCY electrode was

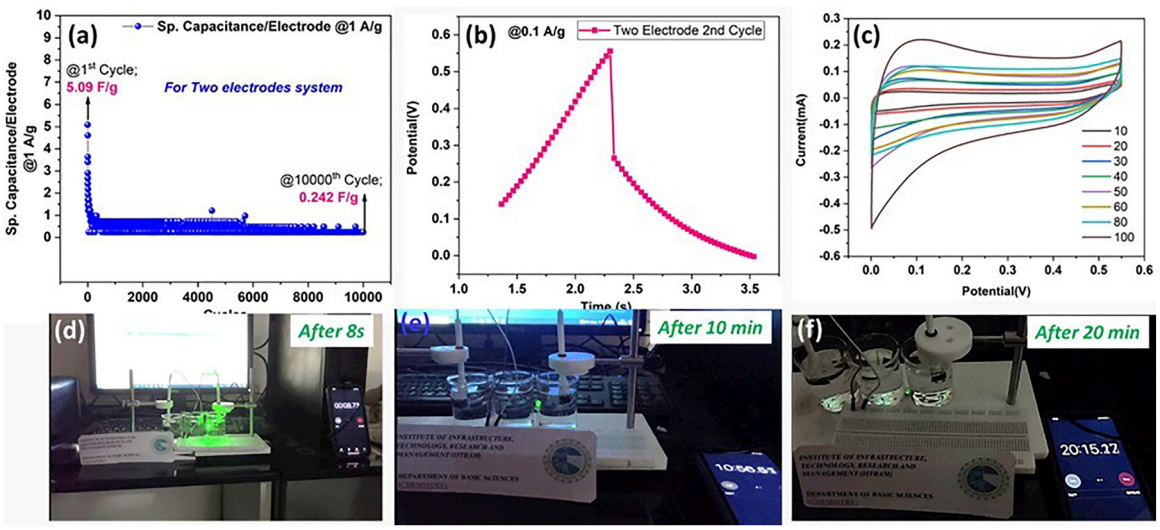

Fig. 8 (a) Cycling performance of the symmetric two-electrode device over 10 000 cycles; (b) galvanostatic charge–discharge (GCD) curve at 0.1 A g^{-1}; (c) cyclic voltammetry (CV) curves at different scan rates (mV s^{-1}); and (d-f) demonstration of three symmetric cells connected in series powering a light-emitting diode (LED) for ~20 min, highlighting the practical applicability of the assembled device.

96.81–99% over 10 000 cycles, indicating the remarkable reversibility of the as-prepared sample. The energy density and power density were calculated using the following equations:[86]

$$E = 1/2C_sV^2 \quad (13)$$

and

$$P = E/t \quad (14)$$

Accordingly, the calculated energy and power densities were 0.924 (KOH), 0.788 (NaOH), and 0.425 (LiOH) Wh kg^{-1} at 27.7, 27.8, and 27.8 W kg^{-1}, respectively. Surprisingly, the power densities were nearly the same across all electrolytes. Despite differences in ionic conductivity among the electrolytes, the equivalent series resistance (ESR) is nearly the same, leading to similar discharge times.

While three-electrode measurements are useful for understanding intrinsic electrode behavior, it is imperative to assess practical device performance within a two-electrode configuration.

In this regard, we conducted symmetric two-electrode device measurements (Fig. 8a–f) in 1 M KOH solution. The device shows stable charge–discharge behavior and characteristic capacitive response, confirming its practical applicability. As expected, the specific capacitance in the two-electrode configuration (5.09 F g^{-1}@1 A g^{-1}) is lower than that observed in the three-electrode system (12.36 F g^{-1}@1 A g^{-1}) due to more realistic operational conditions. The specific capacitance of the symmetric two-electrode cell was calculated using the equation described in Ref. 87, where m represents the total mass of active material from both electrodes. The assembled device demonstrates good cycling stability over 10 000 cycles (Fig. 8a), along with consistent GCD profiles (Fig. 8b) and CV behavior at different scan rates (Fig. 8c). Furthermore, a proof-of-concept demonstration using three devices connected in series successfully powers an LED for approximately 20 minutes (Fig. 8d–f), highlighting the real-world applicability of the system. These findings clearly validate the electrochemical performance of the CCY-based device under practical two-electrode conditions.

5. Conclusion

This study presents a scalable coordination-precursor strategy for engineering a rare-earth-modified, Pt-free Co@CoO–Y_2O_3 heterostructure that integrates alkaline oxygen-reduction catalysis with battery-type supercapacitor functionality. The pyrolysis of a well-defined Co–Y single-crystal precursor produces an intimate multiphase architecture consisting of metallic Co, CoO, and Y_2O_3 with nanoscale domains, abundant heterointerfaces, and hierarchical mesoporosity. Structural and spectroscopic analyses confirmed the formation of a Co@CoO core–shell structure electronically influenced by Y_2O_3, with Raman features suggesting defect- and interface-related interactions.

The composite demonstrated considerable electrocatalytic activity for the ORR with a half-wave potential of 0.603 V, limiting current density of 0.72 mA cm^{-2}, and Tafel slope value of 85.82 mV dec^{-1}, indicating fast ORR kinetics. Moreover, the Co@CoO–Y_2O_3 electrode exhibited a superior energy-storage performance, remaining at ~64.14% of its initial specific capacitance after 10 000-charge–discharge cycles in the KOH at 1 A g^{-1} electrolyte, indicating outstanding cycling stability. Such strong performance is further validated by practical device-level evaluations using symmetric two-electrode device testing in 1 M KOH (5.09 F g^{-1}@1 A g^{-1}), which demonstrate stable CV/GCD behaviour over 10 000 cycles and are capable of powering an LED for about 20 minutes when three cells are linked in series. Overall, this work provides a deliberate configuration of rare-earth modulation of Co/CoO heterointerfaces that couple the selective two-election ORR with robust battery-type alkaline charge storage, representing an attractive avenue for multifunctional materials capable of bridging energy conversion and storage within a single, reproducible platform.

Conflicts of interest

There is no conflict of interest to declare.

Data availability

All characterization data and raw experimental results are included within the manuscript and supplementary information (SI). Supplementary information is available. The additional relevant data supporting the findings of this study are available from the corresponding author upon reasonable request. See DOI: https://doi.org/10.1039/d6ma00229c.

Acknowledgements

The authors gratefully acknowledge Prof. Ashwini Kumar Sharma, IIT Roorkee, for helping with the BET analysis measurement. S. B. S., J. A. B., S. P. and S. D. are grateful to the IITRAM for infrastructure and funding. S. G. would like to greatly acknowledge the Central Research Facility, Chemistry Department, COIR-EV, COI/CNGMT of KIIT Deemed University for their support. J. L. acknowledges the financial support from the Basic Science Research Program (RS-2025-16064308) funded by the National Research Foundation of Korea (NRF), supported by the Ministry of Science, ICT & Future Planning.

References

1 C. Madan, S. Kumari and A. Halder, *Optical Properties of Metal Oxide Nanostructures*, Springer, 2023, pp. 291–330.
2 R. Kadam, M. Yewale, A. Teli, U. Nakate, V. Kumar, S. Kadam and D. Shin, *Surf. Interfaces*, 2023, **41**, 103267.
3 B. Raut, M. S. Ahmed, H.-Y. Kim, M. M. Rahman Khan, G. A. R. Bari, M. Islam and K.-W. Nam, *Batteries*, 2025, **11**, 60.
4 F. Lu, Y. Ji, D. Shi, P. Zhang, S. Zhang, S. Wang and B. Zhang, *J. Energy Storage*, 2024, **84**, 110628.

5 Y. Liu, H. Jiang, J. Hao, Y. Liu, H. Shen, W. Li and J. Li, *ACS Appl. Mater. Interfaces*, 2017, **9**, 31841–31852.
6 X. Zhang, X.-G. Wang, Z. Xie and Z. Zhou, *Green Energy Environ.*, 2016, **1**, 4–17.
7 S. Ingavale, M. Gopalakrishnan, C. M. Enoch, C. Pornrungroj, M. Rittiruam, S. Praserthdam, A. Somwangthanaroj, K. Nootong, R. Pornprasertsuk and S. Kheawhom, *Small*, 2024, **20**, 2308443.
8 M. K. Debe, *Nature*, 2012, **486**, 43–51.
9 Q. Yu, N. Fan, Y. Chang, A. Xu, M. Jia and J. Jia, *J. Alloys Compd.*, 2024, **988**, 174239.
10 X. Wang, M. Li, P. Wang, D. Sun, L. Ding, H. Li, Y. Tang and G. Fu, *Small Methods*, 2023, **7**, 2300100.
11 R. Luo, R. Wang, Y. Cheng, Z. Meng, Y. Wang, Z. Guo, B. B. Xu, Y. Xia and H. Tang, *Adv. Funct. Mater.*, 2024, **34**, 2311084.
12 X. Man, Y. Chang, S. Guo, M. Jia and J. Jia, *J. Rare Earths*, 2025, **43**, 73–80.
13 Y. Li, Q. Liu, T. Li, H. Bi and Z. Shen, *Chin. Chem. Lett.*, 2025, **36**, 110698.
14 S. B. Jaffri, K. S. Ahmad, I. Abrahams, C. J. Kousseff, C. B. Nielsen and B. O. Almutairi, *Int. J. Hydrogen Energy*, 2023, **48**, 29119–29141.
15 R. Luo, R. Wang, Z. Meng, Y. Xia and H. Tang, *Adv. Compos. Hybrid Mater.*, 2023, **6**, 105.
16 F. Liu, X. Lu, C. Shi, D. Wang, T. Cui and Z. Sun, *Chem. Eng. J.*, 2025, 169780.
17 L. Lv, D. Zha, Y. Ruan, Z. Li, X. Ao, J. Zheng, J. Jiang, H. M. Chen, W.-H. Chiang and J. Chen, *ACS Nano*, 2018, **12**, 3042–3051.
18 T. K. Shivasharma, R. Sahu, M. Thosare, D. Sarker, U. Deshpande and B. R. Sankapal, *Sci. Rep.*, 2025, **15**, 28406.
19 Y. Wang, Z. Wang and G. Hu, *Renewable Energy*, 2023, **219**, 119432.
20 S. Prabu, G. Nagaraju, S. Sengodan and K.-Y. Chiang, *Chem. Eng. J.*, 2024, **502**, 158014.
21 S. Gaddimath, S. Aralekallu, K. P. CP, S. Daniel and L. K. Sannegowda, *Int. J. Hydrogen Energy*, 2024, **110**, 181–207.
22 Y. Jiang, L. Chen, H. Zhang, Q. Zhang, W. Chen, J. Zhu and D. Song, *Chem. Eng. J.*, 2016, **292**, 1–12.
23 A. George and M. Kundu, *Energy Fuels*, 2022, **36**, 12327–12340.
24 A. George and M. Kundu, *ACS Omega*, 2023, **8**, 17028–17042.
25 R. Arulraj, A. George and M. Kundu, *ACS Appl. Nano Mater.*, 2024, **7**, 14297–14309.
26 X. Fu, T. Ren, S. Jiao, Z. Tian, J. Yang and Q. Li, *J. Energy Chem.*, 2023, **83**, 397–422.
27 L. Chai, R. Li, Y. Sun, K. Zhou and J. Pan, *Adv. Mater.*, 2025, **37**, 2413658.
28 Z. Zhen, Z. Jiang, X. Tian, L. Zhou, B. Deng, B. Chen and Z.-J. Jiang, *RSC Adv.*, 2018, **8**, 14462–14472.
29 C. Jia, Q. Sun, R. Liu, G. Mao, T. Maschmeyer, J. J. Gooding, T. Zhang, L. Dai and C. Zhao, *Adv. Mater.*, 2024, **36**, 2404659.
30 B. E. Conway, *Electrochemical supercapacitors: scientific fundamentals and technological applications*, Springer, 2013.
31 Y. Jiang and J. Liu, *Energy Environ. Mater.*, 2019, **2**, 30–37.
32 S. A. Pawar, D. S. Patil, J. C. Shin and H. J. Kim, *J. Electroanal. Chem.*, 2020, **873**, 114370.
33 A. González, E. Gómez, A. Cortés-Lozada, S. Hernández, T. Ramírez-Apan and A. Nieto-Camacho, *Chem. Pharm. Bull.*, 2009, **57**, 5–15.
34 E. M. Manohar, S. Roy, S. Bandyopadhyay, M. Pal, S. Singh, V. Ganesan, R. Pełka, P. Konieczny, M. Rams and H. Choi, *Cryst. Growth Des.*, 2024, **24**, 1032–1041.
35 S. B. Samanta, S. Roy, P. Konieczny, R. Pełka, S. Baran, M. Himchan, A. Dey, J. Lee and S. Das, *Dalton Trans.*, 2025, **54**, 16492–16507.
36 Q. Li, Z. Wang and X. Wang, *Micromachines*, 2024, **15**, 154.
37 F. Unal, E. Alp and K. Kazmanli, *J. Chin. Chem. Soc.*, 2022, **69**, 1744–1753.
38 X. Wang, L. Zhao, X. Li, J. Mu, L. Wei, S. Fan, Z. Yin, L. Wang, M. O. Tade and S. Liu, *ACS Sustainable Chem. Eng.*, 2021, **9**, 6107–6117.
39 O. Yıldırım, D. Hilliard, S. S. P. K. Arekapudi, C. Fowley, H. Cansever, L. Koch, L. Ramasubramanian, S. Zhou, R. Böttger and J. R. Lindner, *ACS Appl. Mater. Interfaces*, 2020, **12**, 9858–9864.
40 R. K. Singh, J. C. Douglin, L. Jiang, K. Yassin, S. Brandon and D. R. Dekel, *Energies*, 2023, **16**, 3425.
41 A. Monshi, M. R. Foroughi and M. R. Monshi, *WJNSE*, 2012, **2**, 154–160.
42 A. Alshanableh, Y. S. Ocak, B. Aljawrneh, B. A. Albiss, K. Shawakfehc, L. U. Khane, M. Harfouchee and S. Alrousan, *RSC Adv.*, 2024, **14**, 21180–21189.
43 X. Huang, J. Song, M. Hua, Z. Xie, S. Liu, T. Wu, G. Yang and B. Han, *Green Chem.*, 2020, **22**, 843–849.
44 Q. Li, M. Fan, H. Tang, Y. Zhu, X. Huang, H. Zhang, H. Tang and H. Pan, *J. Colloid Interface Sci.*, 2025, **695**, 137732.
45 M. M. Abo-Zeid, M. G. A. El-Moghny, H. Shawkey, A. Daher, A. M. Abdelkader and M. S. El-Deab, *J. Appl. Electrochem.*, 2024, **54**, 467–485.
46 M. Smyrnioti and T. Ioannides, *Cobalt*, 2017, **49**, 5772.
47 M. C. Biesinger, B. P. Payne, A. P. Grosvenor, L. W. Lau, A. R. Gerson and R. S. C. Smart, *Appl. Surf. Sci.*, 2011, **257**, 2717–2730.
48 H. Feizi, R. Bagheri, Z. Song, J.-R. Shen, S. I. Allakhverdiev and M. M. Najafpour, *ACS Sustainable Chem. Eng.*, 2019, **7**, 6093–6105.
49 Y. Tang, L. Ma, J. Dou, C. M. Andolina, Y. Li, H. Ma, S. D. House, X. Zhang, J. Yang and F. F. Tao, *Phys. Chem. Chem. Phys.*, 2018, **20**, 6440–6449.
50 Y. G. Zhu, Y. Wang, Y. Shi, Z. X. Huang, L. Fu and H. Y. Yang, *Adv. Energy Mater.*, 2014, **4**, 1301788.
51 P. J. Morankar, R. U. Amate, A. M. Teli, A. A. Patil, S. A. Beknalkar and C.-W. Jeon, *Gels*, 2025, **11**, 867.
52 H. Gao, J. Zhang, B. Joshi, E. Samuel, M. Park, M. W. Lee and S. S. Yoon, *J. Alloys Compd.*, 2025, 183511.
53 W. Lu, L. Yan, W. Ye, J. Ning, Y. Zhong and Y. Hu, *J. Mater. Chem. A*, 2022, **10**, 15267–15296.
54 X. Zhang, X. Liu, Y. Zeng, Y. Tong and X. Lu, *Small Methods*, 2020, **4**, 1900823.

55 V. Hadjiev, M. Iliev and I. Vergilov, *J. Phys. C: Solid State Phys.*, 1988, **21**, L199.
56 Y. Repelin, C. Proust, E. Husson and J. Beny, *J. Solid State Chem.*, 1995, **118**, 163–169.
57 A. Ubaldini and M. M. Carnasciali, *J. Alloys Compd.*, 2008, **454**, 374–378.
58 O. Diéguez, O. González-Vázquez, J. C. Wojdeł and J. Íñiguez, *Phys. Rev. B: Condens. Matter Mater. Phys.*, 2011, **83**, 094105.
59 M. Thommes, K. Kaneko, A. V. Neimark, J. P. Olivier, F. Rodriguez-Reinoso, J. Rouquerol and K. S. Sing, *Pure Appl. Chem.*, 2015, **87**, 1051–1069.
60 E. Budiyanto and H. Tüysüz, *Eur. J. Inorg. Chem.*, 2022, e202200065.
61 K. S. Sing, *Pure Appl. Chem.*, 1985, **57**, 603–619.
62 K. Ding, Y. Ye, J. Hu, L. Zhao, W. Jin, J. Luo, S. Cai, B. Weng, G. Zou and H. Hou, *Nanomicro Lett.*, 2023, **15**, 28.
63 C. Ponce de Leon and R. Field, *J. Appl. Electrochem.*, 2000, **30**, 1087–1090.
64 Y. Jiang, T. Fu, J. Liu, J. Zhao, B. Li and Z. Chen, *RSC Adv.*, 2022, **12**, 4805–4812.
65 N. Dhanda, Y. K. Panday and S. Kumar, *Electrochim. Acta*, 2024, **481**, 143872.
66 Z. Jia, G. Yin and J. Zhang, *Rotating electrode methods and oxygen reduction electrocatalysts*, Elsevier, 2014, pp. 199–229.
67 W. Xing, G. Yin and J. Zhang, *Rotating electrode methods and oxygen reduction electrocatalysts*, Elsevier, 2014.
68 N. Talukder, Y. Wang, B. B. Nunna and E. S. Lee, *Catalysts*, 2022, **12**, 791.
69 Y. Ju, W. Huang, Z. Gao, M. Liu and N. Huang, *Appl. Mater. Today*, 2025, **42**, 102576.
70 L. Hu, F. Yu, H. Yuan, G. Wang, M. Liu, L. Wang, X. Xue, B. Peng, Z. Tian and B. Dai, *Chin. Chem. Lett.*, 2019, **30**, 624–629.
71 M. Nunes, D. M. Fernandes, M. Morales, I. Rodríguez-Ramos, A. Guerrero-Ruiz and C. Freire, *J. Appl. Electrochem.*, 2019, **49**, 693–703.
72 D. Zhang, X. Guo, X. Tong, Y. Chen, M. Duan, J. Shi, C. Jiang, L. Hu, Q. Kong and J. Zhang, *J. Alloys Compd.*, 2020, **837**, 155529.
73 Q. Cheng, T. Yang, M. Li and C. K. Chan, *Langmuir*, 2017, **33**, 9271–9279.
74 C. N. Rowley and B. t Roux, *J. Chem. Theory Comput.*, 2012, **8**, 3526–3535.
75 J. Burrow, 2018, https://scholarworks.uark.edu/cheguht/124.
76 A. Kumar, N. Kumar, Y. Sharma, J. Leu and T. Y. Tseng, *Nanoscale Res. Lett.*, 2019, **14**, 266.
77 M. J. Jimenez, M. A. Maria, L. M. Leidens, A. F. Fonseca, M. A. Pereira-da-Silva, V. Rodrigues, F. Alvarez and A. Riul Jr, *ACS Omega*, 2025, **10**, 50611–50625.
78 A. Roy, F. E. Cancino-Gordillo, S. Saha, U. Pal and S. Das, *Int. J. Energy Res.*, 2021, **45**, 14021–14033.
79 Z. Li, Q. Ma, H. Zhang, Q. Zhang, K. Zhang, H. Mei, B. Xu and D. Sun, *Inorg. Chem.*, 2022, **61**, 12129–12137.
80 N. Roy, G. Rajasekhara Reddy, M. R. Pallavolu, R. R. Nallapureddy, M. Dhananjaya, A. Sai Kumar, A. N. Banerjee, B.-K. Min, H. R. Barai and S. W. Joo, *ACS Appl. Mater. Interfaces*, 2024, **16**, 34859–34879.
81 L. G. Ghanem, M. A. Hamza, M. M. Taha and N. K. Allam, *J. Energy Storage*, 2022, **52**, 104850.
82 C. Zhao, W. Zheng, X. Wang, H. Zhang, X. Cui and H. Wang, *Sci. Rep.*, 2013, **3**, 2986.
83 H. Raha, D. Pradhan and P. K. Guha, *J. Electroanal. Chem.*, 2023, **931**, 117193.
84 A. R. Lone, A. Raza, S. Hussain, B. Ramzan, M. K. Khan, K. Sayeed, S. Naseem, K. Pandey and A. Ahmad, *J. Alloys Compd.*, 2025, **1025**, 180384.
85 Q. Liu, H. Xu, Z. He, C. Wei, Z. Wang, G. Li and J. Gao, *Inorg. Chem.*, 2024, **63**, 1550–1561.
86 S. Giri, D. Ghosh and C. K. Das, *Adv. Funct. Mater.*, 2014, **24**, 1312–1324.
87 S. A. Melchior, K. Raju, I. S. Ike, R. M. Erasmus, G. Kabongo, I. Sigalas, S. E. Iyuke and K. I. Ozoemena, *J. Electrochem. Soc.*, 2018, **165**, A501.